X-ray impact on the protoplanetary disks around T Tauri stars

Aresu, G.; Kamp, I.; Meijerink, R.; Woitke, P.; Thi, W. -F.; Spaans, M.

Published in:
Astronomy & astrophysics

DOI:
10.1051/0004-6361/201015449

Publication date:
2011

A&A 526, A163 (2011)
DOI: 10.1051/0004-6361/201015449

Astronomy & Astrophysics

X-ray impact on the protoplanetary disks around T Tauri stars

G. Aresu[1], I. Kamp[1], R. Meijerink[2], P. Woitke[3,4,5], W.-F. Thi[5,6], and M. Spaans[1]

[1] Kapteyn Astronomical Institute, Postbus 800, 9700 AV Groningen, The Netherlands
e-mail: giambattista.aresu@gmail.com
[2] Leiden Observatory, Leiden University, PO Box 9513, 2300 RA, Leiden, The Netherlands
[3] UK Astronomy Technology Center, Royal Observatory, Edinburgh, Blackford Hill, Edinburgh EH9 3HJ, UK
[4] Institute for Astronomy, University of Edinburgh, Royal Observatory, Blackford Hill, Edinburgh EH9 3HJ, UK
[5] Laboratoire d'Astrophysique de Grenoble, CNRS/Université Joseph Fourier (UMR 5571), BP 53, 38041 Grenoble Cedex 9, France
[6] SUPA, Institute for Astronomy, University of Edinburgh, Royal Observatory Edinburgh, UK

Received 22 July 2010 / Accepted 24 November 2010

ABSTRACT

Context. T Tauri stars have X-ray luminosities in the range $L_X = 10^{28} - 10^{32}$ erg s^{-1}. These luminosities are similar to their UV luminosities ($L_{UV} \sim 10^{30}$–10^{31} erg s^{-1}) and therefore X-rays are expected to affect the physics and chemistry of the upper layers of their surrounding protoplanetary disks.

Aims. The effects and importance of X-rays on the chemical and hydrostatic structure of protoplanetary disks are investigated, species tracing X-ray irradiation (for $L_X \geq 10^{29}$ erg s^{-1}) are identified and predictions for [O I], [C II], and [N II] fine structure line fluxes are provided.

Methods. We implemented X-ray physics and chemistry into the chemo-physical disk code ProDiMo. We include Coulomb heating and H_2 ionization as heating processes and both primary and secondary ionization due to X-rays in the chemistry.

Results. X-rays heat the gas causing it to expand in the optically thin surface layers. Neutral molecular species are not significantly affected in terms of their abundance and spatial distribution, but charged species such as N^+, OH^+, H_2O^+, and H_3O^+ display enhanced abundances in the disk surface.

Conclusions. Coulomb heating by X-rays changes the vertical structure of the disk, yielding temperatures of ~8000 K out to distances of 50 AU. The chemical structure is altered by the high electron abundance of the gas at the disk surface, causing an efficient ion-molecule chemistry. The products of this, OH^+, H_2O^+ and H_3O^+, are of great interest for observations of low-mass young stellar objects with the Herschel Space Observatory. Both [O I] (at 63 and 145 μm) and [C II] (at 158 μm) fine structure emission are affected only for $L_X > 10^{30}$ erg s^{-1}.

Key words. protoplanetary disks – methods: numerical

1. Introduction

Young stellar objects emit X-ray radiation (Koyama et al. 1994), which is associated with magnetic coronal processes (Flaccomio et al. 2005; Wolk et al. 2005; Imanishi et al. 2001), jets (Pravdo et al. 2001) mostly producing soft X-rays (Güdel et al. 2007), or outflows launched in the region between the star and the disk as predicted by the X-wind model (Shu et al. 2000). Non-accreting weak-line T Tauri stars (WTTS) are found to be more X-ray luminous than classical accreting T Tauri stars (CTTS) (Stelzer & Neuhäuser 2001; Flaccomio et al. 2003, 2005), because CTTS absorb part of the X-rays in their accretion column (Gregory et al. 2007).

The impact of stellar X-rays on protoplanetary disks around T Tauri stars has been studied by many groups. Glassgold et al. (2004, 2007) found X-rays to be important in heating the surface layers of the disk and estimated the strength of the fine-structure emission lines of [Ne II] and [Ne III], which arise from the warm disk atmosphere exposed to X-ray radiation. Nomura et al. (2007) focused on H_2 level populations and line emission, finding X-rays to control H_2 level population pumping together with UV. Following the work of Meijerink et al. (2008), Ercolano et al. (2008) and Glassgold et al. (2009) studied the atomic-line diagnostics of the inner regions of protoplanetary disks and formation of water in the warm disk atmosphere, respectively. Ercolano et al. (2008) and others focused on the X-ray role in causing the photo-evaporation of the surface layers of the disk. Gorti & Hollenbach (2004, 2008) include X-rays to predict [Ar II, [Ne II], [Fe I], [S I], [Fe II], and [Si II] as good indicators of gas physics in the disk. Woods & Willacy (2009) studied carbon isotope fractionation using the same method as Gorti & Hollenbach (2004) to calculate the X-ray ionization rates. Henning et al. (2010) studied the role of UV and X-rays on C_2H column densities and the excitation conditions in disks around T Tauri stars.

The scope of this paper is to take a step back and first perform a study of the impact of X-rays on the 2D disk structure, on molecular ionized species, and on observational diagnostics such as [O I], [C II], and [N II]. These molecular species were not studied in the above listed previous papers, but are of fundamental interest in the light of their detections with the Herschel satellite (Benz et al. 2010; Bruderer et al. 2010). We undertake an exploratory study of the relative effects of UV and X-rays on the protoplanetary disks hydrostatic, thermal, and chemical structure using a series of X-ray models with different L_X (X-ray luminosity).

2. Model

The chemo-physical disk modeling code ProDiMo (Woitke et al. 2009; Kamp et al. 2010) has been updated with X-ray physics and chemistry.

Table 1. Examples of molecular dissociation and cross-section calculation.

Molecule	Product 1	Product 2	Cross-section
CO	C^{2+}	O	$\sigma_{CO} = 1/3\sigma_C +$
	C^+	O^+	$1/3(0.5\sigma_C + 0.5\sigma_O) +$
	C	O^{2+}	$1/3\sigma_O$
CH	C^{2+}	H	$\sigma_{CH} = \sigma_C$

Notes. CO dissociation can end up in three different channels, which are summed to give the total CO cross-section, CH is only assumed to follow one path. Molecules included: H_2, CH, NH, OH, CN, CO, N_2, SiH, NO, O_2, SiO, CH_2, NH_2, H_2O, HCN, CO_2.

2.1. Input spectrum

The incident stellar spectrum used in Woitke et al. (2009) is composed of a solar model with $T_{\rm eff} = 5800$ K and the cromospheric fluxes of HD 129 333 (Dorren & Guinan 1994). The UV luminosity between 91.2 and 205 nm is $L_{\rm UV} \sim 4 \times 10^{31}$ erg s^{-1}. Different models for the X-ray input spectrum are adopted in the literature: Nomura et al. (2007) use a two-temperature thin thermal-plasma model to fit the observed TW Hydrae spectrum; Ercolano et al. (2008) compiled synthetic coronal spectra using line and continuum emissivities from the CHIANTI compilation of atomic data; Gorti & Hollenbach (2008) use a thermal blackbody. We place the X-ray source on the star and follow Glassgold et al. (1997) and Igea & Glassgold (1999) in using an analytic input spectrum to describe the bremsstrahlung emission from an isothermal plasma $F(E) \propto 1/E \cdot \exp(-E/kT_{\rm X})$ where E is the photon energy between 0.1 and 100 keV, $kT_{\rm X} = 1$ keV, and $T_{\rm X}$ is the plasma temperature. The X-ray input spectrum is added to the input spectrum shown in Fig. 2 in Woitke et al. (2009).

2.2. X-ray chemistry

The following paragraphs describe the implementation of primary and secondary ionization in the code. Forty-one primary ionization reactions and 16 secondary ionization reactions were added to the chemical network.

Primary ionization

The primary rates for X-ray absorption are calculated following Meijerink & Spaans (2005) (Appendix D.3.1). The cross-sections are taken from Verner & Yakovlev (1995). Since X-rays are likely to be absorbed in the K-shells, we assume that every X-ray absorption leads to a single ionization for H, He, Si, and Cl and a double ionization for C, N, O, S, and Fe (Meijerink & Spaans 2005). We take into account molecular X-ray absorption, which always leads to dissociation, of the species. Table 1 lists two examples of how the total dissociation rates are calculated. When the difference in weight of the elements that form the molecule is large (e.g. CH, OH, H_2O etc.), we use the cross-section of the heavier element, when the weight is comparable (e.g. CO, CN, NO etc.) we combine the cross-sections of the single elements.

Secondary ionization

The fast electrons generated by the X-ray absorption can further ionize the gas. The rates are computed as shown in Meijerink & Spaans (2005, Appendix D.3.2) using experimental data from Lennon et al. (1988). The volumetric rates are a function of the local chemistry, i.e. they depend on the species densities $n_{\rm H}$, $n_{\rm H_2}$, $n_{\langle \rm H \rangle}$, and $n_{\rm e}$ (where n_H is the hydrogen atom density and $n_{\langle \rm H \rangle}$ is the hydrogen nuclei density). This has to be taken into account when solving the chemical equilibrium. The additional entries in the chemical Jacobian that come from the X-ray secondary ionization reactions are implemented following Sect. 5.6 in Woitke et al. (2009).

Table 2. Parameters used in the models: the X-ray luminosity values correspond to the `models 1-5`.

Quantity	Symbol	Value
Stellar mass	M_*	1 $M_\odot$
Stellar luminosity	L_*	1 $L_\odot$
Disk mass	$M_{\rm disk}$	0.01 $M_\odot$
X-ray luminosity (0.1−50 keV)	$L_{\rm X}$	$0, 10^{29}, 10^{30}$ $10^{31}, 10^{32}$
Inner disk radius	$R_{\rm in}$	0.5 AU
Outer disk radius	$R_{\rm out}$	500 AU
Surface density power law index	ϵ	1.5
Min. dust particle size	$a_{\rm min}$	0.1 μm
Max. dust particle size	$a_{\rm max}$	10 μm
Dust size distribution power index	$a_{\rm pow}$	2.5

2.3. X-ray heating

We added Coulomb heating (Dalgarno et al. 1999) and H_2 ionization heating (Meijerink & Spaans 2005, Appendix B.1) to the heating processes listed in Woitke et al. (2009). The Maloney et al. (1996) heating rate holds only for gas with low $x_{\rm e}$, while Dalgarno et al. (1999) present the more general case for different high and low ionization gases (atomic/molecular). The heating efficiency increases by a factor of 7−8 in a highly ionized atomic gas and a factor of 2 in a highly ionized molecular gas (Shull & van Steenberg 1985).

2.4. Parameter space

We computed five different models with increasing $L_{\rm X}$ to compare the results with the UV only case (`model 1`) for a disk surrounding a T Tauri star (Table 2). In `model 1`, X-rays are switched off. This is the model presented in Woitke et al. (2009). For more details, we refer to the original paper. X-ray models (`model 2−5`) have the same parameters as `model 1`, but include stellar X-rays ($L_{\rm X} = 10^{29} - 10^{32}$ erg s^{-1}). We added Cl, Cl^+, and double ionized species (C^{2+}, N^{2+}, O^{2+}, S^{2+}, Fe^{2+}) to the chemical network. The X-ray emission is treated as a point source at the location of the star.

3. Results

We analyze the results obtained from the five models described above. We first present the thermal and hydrostatic structure of the various models. We then describe the impact of X-rays on the chemistry and fine-structure line emission, focusing on the main differences between the UV-only model and the combined UV+X-ray models.

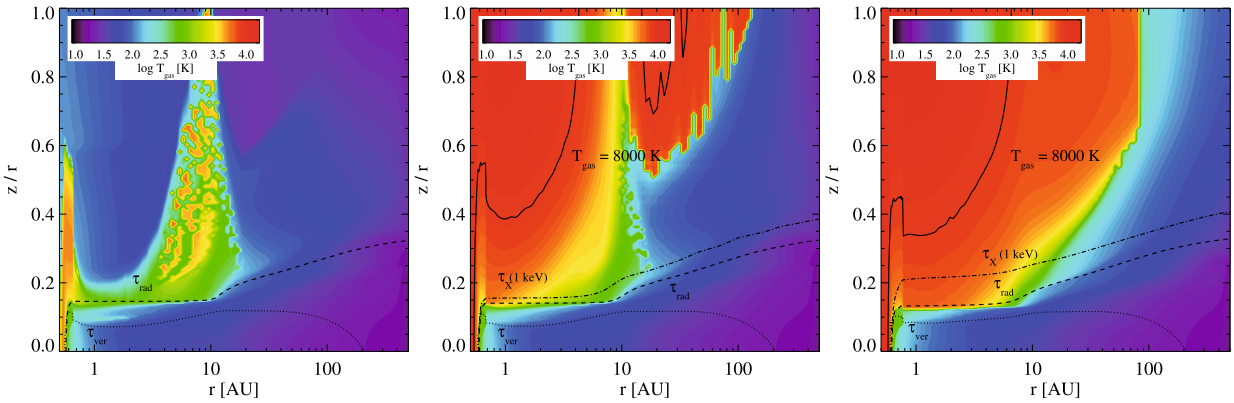

Fig. 1. Gas temperature distribution: `Model 1` (UV only) in the *left panel*, X-ray models with $L_X = 10^{30}$ erg s^{-1} (`model 3`), $L_X = 10^{32}$ erg s^{-1} (`model 5`) in the *middle and right panel*, respectively. Contour lines are plotted over for $\tau_{rad} = 1$ (radial dust optical depth at 550 nm, dashed line), $\tau_{ver} = 1$ (vertical dust optical depth at 550 nm, dotted line), and an X-ray optical depth of one at 1 keV (dot-dashed line). The relative positions of these two depths depend strongly on the assumed dust properties (see Table 2). The solid line corresponds to $T_{gas} = 8000$ K.

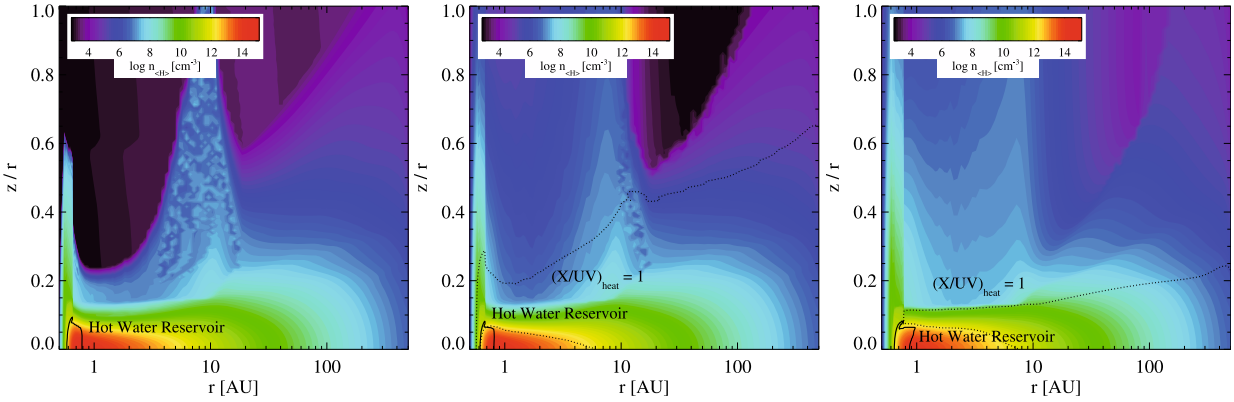

Fig. 2. Total hydrogen nuclei density $n_{\langle H \rangle}$ distribution: `Model 1` (UV only) in the *left panel*, X-ray models with $L_X = 10^{30}$ erg s^{-1} (`model 3`), $L_X = 10^{32}$ erg s^{-1} (`model 5`) in the *middle and right panels*, respectively. The dotted contour line shows where the ratio of Coulomb heating to photo-electric plus PAH heating equals 1. The solid line encircles the hot water reservoir ($T_{H_2O} > 200$ K).

Temperature and density structure

The low density ($n_{\langle H \rangle} < 10^8$ cm^{-3}) surface layers directly exposed to X-ray radiation are heated efficiently by means of Coulomb heating: in all X-ray models, temperatures reach ~8000 K (Fig. 1). The extension of this high temperature region increases with L_X: it reaches 2 AU in `model 2` and 100 AU in `model 3` and `4`. In `model 5`, the temperature is slightly lower for $r > 50$ AU but the whole disk is warmer (Fig. 1). X-rays dominate the thermal balance only in the upper layers down to $(X/UV)_{heat} = 1$. Beyond $(X/UV)_{heat} = 1$, UV heating takes over and becomes the main heating process. Deeper within the midplane, both X-ray and UV heating are negligible, but their ratio is again inverted and harder X-rays ($E > 10$ keV) deposit more energy than UV radiation (Fig. 2).

The inner wall of the disk is always directly illuminated by the stellar radiation causing the inner rim (0.5 AU $< r <$ 0.7 AU) to have a large scale-height and hence vertical extent. In the UV model, the shadowed disk atmosphere beyond the inner rim has a lower vertical scale-height since radiation cannot penetrate efficiently and sustain high gas temperatures. Only radiation that impinges the disk at higher angles ($z/r > 0.6$) and scattered radiation reach the outer disk causing the temperature to increase and consequently the production of a second bump at ~9 AU. When X-rays are switched on, the temperature increase in the surface layers directly affects the vertical density distribution there since we keep the radial surface density profile fixed. The inner rim of the disk ($r < 1$ AU and $z/r > 0.1$) is more puffed up (Fig. 2). The second bump at ~9 AU is also more vertically extended; in `model 5`, it even "merges" with the inner rim and flares as a whole (Fig. 2, third panel).

Chemistry

The abundances of neutral molecules such as CO, OH, and H_2O generally change by less than an order of magnitude over the entire modeling space. On the other hand, the ion chemistry in the disk surface strongly changes: the electron abundance in the upper layers increases by a factor of 10^4. This leads to an enhancement in the OH^+, H_2O^+, H_3O^+, and N^+ abundances. Secondary ionization of H_2 increases the H_2^+ abundances. H_2^+ collisions with H_2 produce H_3^+. Subsequent collisions of H_3^+ with O, OH, and H_2O lead to the production of OH^+, H_2O^+, and H_3O^+, respectively. Figure 4 shows how the vertical column densities of these species change with L_X for three different disk radii: 3, 10, and 100 AU. Both OH^+ and H_2O^+ respond more efficiently than H_3O^+ to the X-ray radiation as the total mass ratio $M(OH^+)/M(H_2O^+)$ only doubles from `model 1` to `model 5`, while $M(OH^+)/M(H_3O^+)$ increases by more than a factor of 5.

OH^+: OH^+ formation is enhanced approximately proportionally to the X-ray luminosity. Its total mass increases from 8×10^{-15} $M_\odot$ in `model 1` by a factor of 3.6 in `model 3` to about a factor of 500 in `model 5` (Table 4).

Table 3. Predicted line fluxes of [O I] at 63 μm, [C II] at 157 μm and [N II] at 205 μm for all the models expressed in W/m^2.

Line	Model 1	Model 2	Model 3	Model 4	Model 5
[O I] 63 μm	4.8(–17)	4.6(–17)	4.8(–17)	8.3(–17)	3.6(–16)
[O I] 145 μm	1.5(–18)	1.3(–18)	1.4(–18)	2.3(–18)	1.2(–17)
[C II] 157 μm	1.5(–17)	1.5(–17)	1.7(–17)	3.0(–17)	6.1(–17)
[N II] 205 μm	3.6(–26)	5.2(–23)	4.6(–22)	4.1(–21)	1.1(–20)

Notes. All fluxes are computed for a distance of 140 pc.

As the X-ray luminosity increases, OH^+ formation is enhanced and pushed outwards, where the disk is colder. The column density of OH^+ increases substantially beyond $r > 10$ AU in all models. It reaches ~100 times its initial value (model 1) in model 3 at 100 AU (Fig. 4).

H_2O^+: The H_2O^+ mass increases by a factor of 3 (a factor of 100) between model 1 and model 3 (and Model 5). The column density again increases toward the outer part of the disk. Model 3 has ~10 times higher column density than Model 1 at both 10 and 100 AU. As for OH^+, H_2O^+ appears to move toward the outer part of the disk with increasing X-ray luminosity.

H_3O^+: The H_3O^+ mass is slightly less affected by X-rays: it is two times higher than in the UV case in model 3 and ten times in model 4. In model 3, model 4, and model 5, the region of high H3O+ abundances is also clearly pushed to larger radii and hence the species mass averaged temperature becomes lower.

N^+: We find the most extreme mass increase for N^+ in all X-ray models (Table 4) and at all radii: in model 3, it is 1000 times higher than in the UV-only case.

In models 4 and 5, the N^+ mass increases over-proportionally in the outer part of the disk (Fig. 4, right lower panel). Figure 5 shows the column density ratio of the X-ray dominated N^+ to the UV dominated C^+. With increasing L_X, the N^+ column density is enhanced by two (outer disk) to six (inner disk) orders of magnitude.

Line predictions

In Table 3, we list the flux prediction of [O I] 63 μm, [O I] 145 μm, [C II] 157 μm, and [N II] 205 μm for all the models. Figure 3 shows their values as a function of the X-ray luminosity. The [N II] line flux shows the strongest correlation with the X-ray flux, increasing by five orders of magnitude from model 1 to model 3. The oxygen fine-structure line fluxes and the [C II] line flux are constant from model 1 to 3 (Fig. 3), because they originate in the UV-heated layer. Only in models 4 and 5 do the line fluxes increase with L_X.

4. Discussions and conclusions

We have found that X-rays mainly impact the surface layers of protoplanetary disks. The hydrostatic structure of these layers is changed significantly: X-ray radiation is mostly absorbed in the tenuous layers ($z/r \geq 0.2\,\mathrm{cm}^{-3}$) increasing the temperature to ~8000 K; at those temperatures, cooling by [O I], Fe II, and Lyα balance the X-ray heating. This causes the density structure to flare more strongly than in the UV-only case (Fig. 2).

The general results of Nomura et al. (2007) and Glassgold et al. (2004) are qualitatively confirmed, showing that the inner rim and the surface layers are dominated by X-rays. In addition, we have found that the more distant parts, out to 100 AU, are also affected (Fig. 4). We find that the size of the high temperature

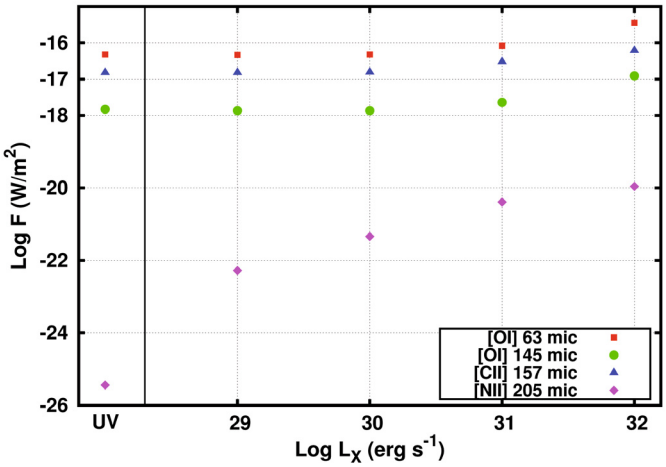

Fig. 3. Oxygen-line flux emission at 63 and 157 μm, ionized carbon-line flux emission at 157 μm and ionized nitrogen-line flux emission at 205 μm as a function of the X-ray luminosity. All fluxes are compiled for a distance of 140 pc. The correlation between N II and L_X is clear, while O I and C II show no correlation for $L_X < 10^{30}$ erg s^{-1}.

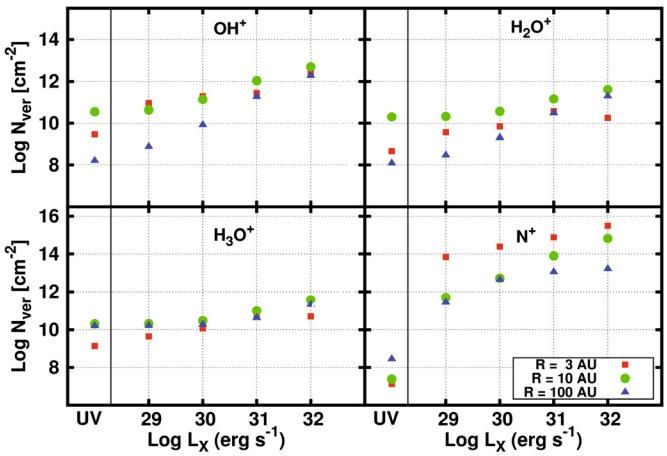

Fig. 4. Column density of OH^+ (*upper left panel*), H_2O^+ (*upper right panel*), H_3O^+ (*lower left panel*), and N^+ (*lower right panel*) at three different radii (3, 10, 100 AU) versus X-ray luminosity. In each panel, the UV-only model is indicated by the "UV" label on the *x*-axis.

X-ray driven region increases with L_X. This is because our model uses the Dalgarno et al. (1999) prescription for X-ray heating and of our choice of the input spectrum. The heating efficiencies of Dalgarno et al. (1999) lead to ~7–8 times higher rates in regions with high electron fraction, than Maloney et al. (1996). Furthermore, our input spectrum has higher photon flux in the range 0.1–0.3 keV than, e.g., Gorti & Hollenbach (2008) and Nomura et al. (2007). These soft X-ray photons are absorbed at low vertical column-densities causing high e^- densities there and are thus more efficient in heating the upper layers. This was also noted in Gorti et al. (2009).

Gorti & Hollenbach (2008) found X-rays to be the dominant heating process in slightly deeper layers than we do. This is most likely because we include UV scattering from dust, which leads to a more substantial vertical penetration of FUV radiation into the disk. Nomura et al. (2007) also show that FUV penetrates deeper than X-rays, because FUV scattering is more efficient than X-ray Compton scattering at 1 keV, which is not included in our model. Gorti & Hollenbach (2008) also consider a less steep

Table 4. Species masses given in units of solar mass for all the models.

Species	UV Only	$L = 10^{29}$ erg s^{-1}	$L = 10^{30}$ erg s^{-1}	$L = 10^{31}$ erg s^{-1}	$L = 10^{32}$ erg s^{-1}
H	5.0(−05)	5.0(−05)	5.2(−05)	7.1(−05)	1.4(−04)
H_2	7.6(−03)	7.6(−03)	7.6(−03)	7.6(−03)	7.5(−03)
C	3.0(−07)	3.0(−07)	3.1(−07)	3.4(−07)	4.8(−07)
C+	1.3(−07)	1.3(−07)	1.3(−07)	1.4(−07)	1.8(−07)
O	1.4(−05)	1.4(−05)	1.4(−05)	1.4(−05)	1.4(−05)
CO	9.5(−06)	9.4(−06)	9.3(−06)	9.0(−06)	9.0(−06)
OH	3.4(−11)	3.4(−11)	3.7(−11)	7.0(−11)	2.8(−10)
H_2O	7.7(−07)	4.7(−08)	3.6(−08)	2.7(−08)	3.3(−08)
OH^+	7.9(−15)	1.1(−14)	2.9(−14)	4.1(−13)	4.6(−12)
H_2O^+	1.9(−15)	2.1(−15)	5.3(−15)	6.2(−14)	4.2(−13)
H_3O^+	3.4(−15)	3.7(−15)	7.3(−15)	4.8(−14)	3.5(−13)
N^+	2.9(−15)	8.7(−13)	3.9(−12)	9.9(−12)	3.6(−11)

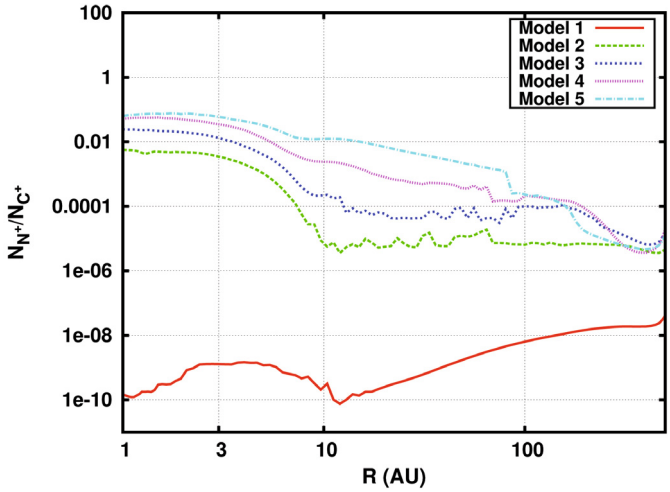

Fig. 5. Column density ratio of the X-ray dominated N^+ to the UV dominated C^+. The latter does not change in the X-ray models with respect to the UV model.

surface-density distribution that yields less mass at 1 AU, where most of the X-ray radiation is absorbed in our model.

The X-ray energy deposition does not affect the neutral oxygen fine-structure emission at 63 and 145 μm (Table 3), unless the X-ray luminosity is pushed to $L_X > 10^{30}$ erg s^{-1}, where X-ray heating dominates in the regions where the emission takes place. Ionized carbon emission at 157 μm is only slightly affected by the X-rays in all the models, as the line emission is dominated by material at $R > 200$ AU (Woitke et al. 2009; Kamp et al. 2010), where the X-ray contribution to the chemistry and thermal balance is negligible. Our values are in good agreement with Meijerink et al. (2008) and Ercolano et al. (2008) for $L_X \sim 10^{30}$ erg s^{-1}. However, the correlation of the oxygen line fluxes with L_X, found in the Meijerink et al. (2008) model is caused by the lack of UV radiation in their model. In our model at low L_X, the UV heating ensures that the gas temperature is sufficiently high to sustain a constant level of [O I] emission.

We have found that the H_2, CO, and OH properties of the X-ray models are largely unvaried with respect to `model 1`. The largest change occurs for water, whose mass diminishes by a factor of 20 in the highest L_X model relative to the UV-only model. The X-rays enhance the electron abundance in the surface layers, where we find that $x_e \sim 0.1$ for $z/r \sim 0.9$ out to 100 AU. Ionized species abundances such as OH^+, H_2O^+, H_3O^+, and N^+, are enhanced. The molecular ionized species form at increasingly greater radii as L_X increases. High abundances of OH^+ and H_2O^+ are a characteristic signature of an X-ray dominated region as discussed by van der Werf et al. (2010) after the detection with Herschel/SPIRE in the ultra-luminous galaxy Mrk 231. Furthermore, this is extremely interesting in the context of the detection of these species in a massive YSO by Herschel (Benz et al. 2010). The column densities that we find from our X-ray irradiated disks are of the same order of magnitude as those derived in Benz et al. (2010). This suggests that a disk could in principle provide a substantial contribution to the line fluxes emitted from these molecules, making our result extremely relevant to future Herschel studies of low-mass YSOs.

The abundance of these ions increases especially at larger radii ($r > 10$ AU), while the N^+ abundance rises considerably at all radii. The latter is not observed in the UV model because of the high ionization potential of N(I.P.) = 14.5 eV. We have found that the N^+ flux emitted at 205 μm in `model 3` is $\sim 5 \times 10^{-22}$ W/m^2, coming for 90% from the upper layers beyond 10 AU. This is much smaller than the current Herschel sensitivity limit of 5×10^{-18} W/m^2 (HIFI, 5σ in 1 h) and even below current sensitivity estimates for SPICA/SAFARI (10^{-19} W/m^2, 5σ in 1 h). We have only considered X-ray ionization, but the flux is unlikely to change if EUV is present. Additional ionization occurs only at smaller radii, because of the low penetration depth of EUV radiation (Hollenbach & Gorti 2009). The formation of molecular ionized species moves toward the outer disk as L_X increases.

5. Outlook

Our predicted N^+ line fluxes are too low to be observed with current instruments. In contrast, the [O I] 63 μm and [C II] 157 μm lines are observable in the presence of UV luminosities of $\sim 10^{31}$ erg s^{-1} and/or strong X-rays ($L_X > 10^{30}$ erg s^{-1}). In the context of the Herschel observatory, the OH^+, H_2O^+, and H_3O^+ lines are extremely interesting as they are likely to be observable with the HIFI, PACS, and SPIRE instruments. These hydride ions and the already observed [Ne II] and [Ar II] line fluxes, will be addressed in a future paper (Aresu et al., in prep.). We will also investigate a larger parameter space and the effect of the change in disk structure – especially of a higher inner rim and greater flaring – on the overall SED. Future work will also include the creation of a grid of X-ray models following the Woitke et al. (2010) approach.

Acknowledgements. The authors acknowledge the anonymous referee for helpful comments that improved the clarity and completeness of the paper. This work has been funded by The Netherlands Organization for Scientific Research

(NWO). The LAOG group acknowledge PNPS, CNES, and ANR (contract ANR-07-BLAN-0221) for financial support.

References

Benz, A. O., Bruderer, S., van Dishoeck, E. F., et al. 2010, A&A, 521, L35
Bruderer, S., Benz, A. O., van Dishoeck, E. F., et al. 2010, A&A, 521, L44
Dalgarno, A., Yan, M., & Liu, W. 1999, ApJS, 125, 237
Dorren, J. D., & Guinan, E. F. 1994, ApJ, 428, 805
Ercolano, B., Drake, J. J., Raymond, J. C., & Clarke, C. C. 2008, ApJ, 688, 398
Flaccomio, E., Micela, G., & Sciortino, S. 2003, A&A, 397, 611
Flaccomio, E., Micela, G., Sciortino, S., et al. 2005, ApJS, 160, 450
Glassgold, A. E., Najita, J., & Igea, J. 1997, ApJ, 480, 344
Glassgold, A. E., Najita, J., & Igea, J. 2004, ApJ, 615, 972
Glassgold, A. E., Najita, J. R., & Igea, J. 2007, ApJ, 656, 515
Glassgold, A. E., Meijerink, R., & Najita, J. R. 2009, ApJ, 701, 142
Gorti, U., & Hollenbach, D. 2004, ApJ, 613, 424
Gorti, U., & Hollenbach, D. 2008, ApJ, 683, 287
Gorti, U., Dullemond, C. P., & Hollenbach, D. 2009, ApJ, 705, 1237
Gregory, S. G., Wood, K., & Jardine, M. 2007, MNRAS, 379, L35
Güdel, M., Telleschi, A., Audard, M., et al. 2007, A&A, 468, 515
Henning, T., Semenov, D., Guilloteau, S., et al. 2010, ApJ, 714, 1511
Hollenbach, D., & Gorti, U. 2009, ApJ, 703, 1203
Igea, J., & Glassgold, A. E. 1999, ApJ, 518, 848
Imanishi, K., Koyama, K., & Tsuboi, Y. 2001, ApJ, 557, 747
Kamp, I., Tilling, I., Woitke, P., Thi, W., & Hogerheijde, M. 2010, A&A, 510, A18
Koyama, K., Maeda, Y., Ozaki, M., et al. 1994, PASJ, 46, L125
Lennon, M. A., Bell, K. L., Gilbody, H. B., et al. 1988, J. Phys. Chem. Ref. Data, 17, 1285
Maloney, P. R., Hollenbach, D. J., & Tielens, A. G. G. M. 1996, ApJ, 466, 561
Meijerink, R., & Spaans, M. 2005, A&A, 436, 397
Meijerink, R., Glassgold, A. E., & Najita, J. R. 2008, ApJ, 676, 518
Nomura, H., Aikawa, Y., Tsujimoto, M., Nakagawa, Y., & Millar, T. J. 2007, ApJ, 661, 334
Pravdo, S. H., Feigelson, E. D., Garmire, G., et al. 2001, Nature, 413, 708
Shu, F. H., Najita, J. R., Shang, H., & Li, Z. 2000, Protostars and Planets IV, 789
Shull, J. M., & van Steenberg, M. E. 1985, ApJ, 298, 268
Stelzer, B., & Neuhäuser, R. 2001, A&A, 377, 538
van der Werf, P. P., Isaak, K. G., Meijerink, R., et al. 2010, A&A, 518, L42
Verner, D. A., & Yakovlev, D. G. 1995, A&AS, 109, 125
Woitke, P., Kamp, I., & Thi, W. 2009, A&A, 501, 383
Woitke, P., Pinte, C., Tilling, I., et al. 2010, MNRAS, 405, L26
Wolk, S. J., Harnden, Jr., F. R., Flaccomio, E., et al. 2005, ApJS, 160, 423
Woods, P. M., & Willacy, K. 2009, ApJ, 693, 1360